Comparisons of High-Linear Energy Transfer Particle Spectra on the ISS and in Deep Space

Cary Zeitlin[1*], Livio Narici[2], Ryan R. Rios[1], A. Rizzo[2], Donald M. Hassler[3],

Bent Ehresmann[3], Robert F. Wimmer-Schweingruber[4], Jingnan Guo[4],

Nathan A. Schwadron[5], Harlan E. Spence[5]

1. Leidos Innovations Corporation, Houston, TX, USA
2. Department of Physics, University of Rome Tor Vergata, Rome, Italy and INFN Tor Vergata, Rome, Italy
3. Southwest Research Institute, Planetary Science Division, Boulder, CO, USA
4. Christian Albrechts University, Department of Extraterrestrial Physics, Kiel, Germany
5. University of New Hampshire, Department of Physics, Dover, NH, USA

* Corresponding author: cary.j.zeitlin@nasa.gov

Abstract.

Aims In deep space, personnel and equipment are exposed to the space radiation environment in the form of energetic particles, specifically Galactic Cosmic Rays and sporadic Solar Energetic Particle events. Radiation fields resulting from these particles are modified by shielding, but most radiation measurements in deep space have been made with detectors that were unshielded or very lightly shielded. In contrast, the space radiation environment on the International Space Station (ISS) is more complicated, with time-dependent modification of the incident flux by the geomagnetic field and complex bulk shielding distributions; measured particle spectra inside the ISS are affected by both types of shielding. The geomagnetic field is also responsible for the existence of the South Atlantic Anomaly, a region of trapped energetic protons and electrons, and hence enhanced radiation dose, through which the ISS travels several times per day on average. Here, our primary aim is to compare charged particle spectra at high linear energy transfer (LET) obtained by the ALTEA detector on ISS during high-latitude portions of the orbit to similar data acquired by the CRaTER and RAD instruments, both in deep space. The comparison has implications for radiation biology; specifically, if the ISS radiation environment – at least at high latitudes – is a reasonable approximation, on average, of the deep-space and/or Mars surface environment, it may offer a superior platform for radiation biology experiments

32 compared to accelerator laboratories where even the lowest dose rates are orders of magnitude
33 higher than those in space.
34
35 _Methods_ CRaTER flies on the LRO spacecraft in lunar orbit, and RAD is part of the Curiosity
36 rover science payload on the surface of Mars. RAD operated for most of its cruise to Mars
37 aboard the MSL spacecraft, during a period in 2012 when ALTEA was in regular operation on
38 the ISS in the USLab. Later in 2012, ALTEA was moved to the Columbus module, while RAD
39 was acquiring data on the surface of Mars. CRaTER operated continuously during both periods.
40 All three instruments report the energy deposition in silicon from charged particles. These energy
41 depositions are used in ground analysis to determine LET spectra in water, which in turn are
42 used to calculate the dosimetric quantities of interest. ALTEA is insensitive to particles with
43 LET's below about 2.5 keV/μm in silicon; the comparisons are therefore restricted to the high-
44 LET region above this threshold.
45
46 _Results_ We find that the high-LET GCR environments measured by ALTEA when ISS is at high
47 latitudes have many features in common with shielded environments outside the
48 geomagnetosphere. In the first period studied, ALTEA was in the USLab module of the ISS and
49 under heavy shielding; the high-LET spectrum it measured is, on average, quite similar to that
50 obtained in the same LET range by RAD on Mars in the later period, under similar heliospheric
51 conditions. The high-LET spectrum obtained by RAD during its cruise to Mars is also found to
52 be very similar to the spectrum seen in the most-shielded CRaTER detectors, and to the ALTEA
53 spectrum obtained in the second period (while in Columbus). These findings may be pertinent to
54 identifying analogues for radiation biology experiments, and we discuss their implications.
55

1. Introduction – the Space Radiation Environment

57 Exposure to energetic particle radiation has long been considered a health risk in the human
58 exploration of deep space (Tobias 1958; Dye & Wilkinson 1965; Curtis & Wilkinson 1968;
59 English et al. 1973). On Earth, there are three fundamental principles of radiation protection:
60 minimize exposure time, maximize both shielding and distance from the source. In space, only
61 the first principle can be applied in practice, principally due to the isotropy and high energies of
62 GCRs. The practical difficulties of shielding against these ions leaves mission duration as the

63   primary means of limiting exposures at present, although in the future, countermeasures

64   including pharmacology and diet may increase allowable durations. Dose rates from galactic

65   cosmic rays (GCRs) are generally modest, but high-energy heavy ions are present, and these

66   have biological effects which are highly uncertain and potentially serious (Cucinotta et al. 2003;

67   Durante & Cucinotta 2008; Cucinotta et al. 2013). Solar Energetic Particle (SEP) events may

68   produce high dose rates, but in most events, the large majority of SEPs are protons with kinetic

69   energies less than 100 MeV, so that modest shielding (e.g., from the hull of a spacecraft)

70   provides sufficient protection (Wilson et al. 1999; Durante & Cucinotta 2011); similarly, modest

71   depths of bulk shielding are effective in reducing the doses received in low-Earth orbit (LEO)

72   during traversals of the South Atlantic Anomaly (SAA). Extreme "hard-spectrum" SEP events,

73   although less common, may produce large fluxes at high energies, and therefore present

74   essentially the same shielding challenges as GCRs (Tylka & Dietrich, 2009).

75

76   Our purpose here is to compare the linear energy transfer (LET) spectra of GCRs observed in

77   deep space with spectra measured using similar instrumentation in LEO aboard the International

78   Space Station (ISS). The comparisons are focused on the high-LET portion of the spectrum,

79   which (using the definition employed here) contains GCR heavy ions and relatively low-energy

80   protons and helium ions. Relative to the deep space radiation environment, the LEO environment

81   is protected by the Earth's magnetic field, though less so at higher magnetic latitudes than lower.

82   In addition, many locations inside the ISS are significantly shielded by the mass of the

83   surrounding modules, equipment racks, etc. By comparing data taken simultaneously by

84   instruments in different heliospheric locations, we can address two important questions: How

85   much are GCR spectra influenced by these differences in magnetic and bulk shielding? And,

86   second, can the high-LET spectrum obtained in LEO at high latitudes serve as a proxy for deep

87   space? The second question has implications for the utility of radiation biology experiments, as

88   well as deep space habitat model validations, that could be carried out on the ISS.

89

90   **2. Instruments**

91   Data acquired in 2012 by the ALTEA (Zaconte et al. 2008), MSL-RAD (Hassler et al. 2012) –

92   which will be referred to simply as RAD throughout this article – and CRaTER (Spence et al.

93   2010) instruments are used in this analysis. All three are based on silicon detector technology,

94 and therefore have many similarities, although the detailed designs and capabilities of the

95 instruments vary as described below. The fact that silicon is the common detection medium

96 allows us to directly compare measurements of LET, or dE/dx, between the instruments.

97 Throughout the following, when we refer to LET, we mean LET in silicon unless stated

98 otherwise. Of the three instruments considered, only ALTEA measures the exact incidence angle

99 of incoming particles and hence gives information about the path length, dx, through the

100 detectors. For CRaTER and RAD, we consider particles in narrow acceptance cones, so that the

101 range of path lengths through the detectors is highly constrained and on average only a few

102 percent larger than that for particles at normal incidence.

103

104 *2.1 General Principles*

105 The instruments used in this analysis are all capable of detecting charged particles in "telescope"

106 geometries. Setting aside some details for the moment, it is generally straightforward to relate

107 measured count rates to particle fluxes via the geometric factor: the integral flux J is given by

108 $$J = N_t / (G \, \varepsilon \, t)$$

109 where N_t is the total number of counts collected in time interval t, ε is the detection efficiency,

110 and G is the telescope's geometric factor (Sullivan 1971), often given in units of cm^2 steradian.

111 Flux is often reported in units of cm^{-2} sr^{-1} sec^{-1}, referred to here as a "pfu" (particle flux unit).

112 Flux can also be presented as differential flux, dJ/dE (in units of cm^{-2} sr^{-1} sec^{-1} MeV^{-1}) when the

113 data have energy resolution.

114

115 In a planar detection geometry – pertinent for all instruments considered here – it can be shown

116 that the dose rate in units of nanoGray (nGy) per unit time is related to the fluence rate by the

117 equation

118 $$D = 1.602 \, \phi \, <L> / \rho \, t$$

119 where ϕ is the fluence in units of particles per cm^2, $<L>$ is the LET averaged over all incident

120 particles in units of keV/μm, ρ is the density of the medium being traversed in units of $g \, cm^{-3}$,

121 and t is the length of time over which the data were collected and the factor 1.602 yields the

122 desired units. To relate dose to flux therefore requires extrapolation from measured integral flux

123 J to fluence ϕ, and this step introduces uncertainties which may be significant. Typically, the

124 problem is simplified by assuming the incident radiation is isotropic; the same assumption is
125 usually made in calculating geometric factors. Assuming isotropy, a multiplicative factor of 4π is
126 sufficient to extrapolate from flux measured in a narrow cone to the full fluence coming from all
127 directions. Using a factor of 4π corresponds to extrapolating from the flux of particles seen in the
128 instrument's viewing cone to a "free space" situation in which particles impinge isotropically.
129 This is not ideal for instruments observing from surfaces or from orbital platforms where a large
130 fraction of the solid angle is shielded by a planetary body; a factor of 2π is more appropriate in
131 those settings. In addition, the accuracy of the extrapolation is only as good as the assumption of
132 isotropy, and there are a few situations in which the assumption is known to be a poor one. For
133 example, during ISS traversals of the South Atlantic Anomaly, the incident radiation is
134 anisotropic, and this is also true in various phases of some SEP events. It is also the case that
135 highly inhomogeneous shielding distributions will produce anisotropic radiation fields. These
136 caveats should be borne in mind when assessing the dose rate data presented in the following.
137
138 Note that the dose calculation requires accurate knowledge of the average LET; in the space
139 radiation environment, this is only possible with a detector that is capable of handling signals
140 over a very wide dynamic range. The relevant LET range goes from about 0.3 keV/μm in silicon
141 for minimum-ionizing, singly-charged particles, to about 500 keV/μm for low-velocity, high-Z
142 ions.
143

144 *2.2 ALTEA*
145 The ALTEA cosmic ray detector (Zaconte et al. 2010a, 2010b; Di Fino et al. 2006, 2011, 2012;
146 Narici et al. 2015, 2017) acquired data onboard the ISS from 2006 to 2012 for a total of about
147 3.5 years. It is composed of six Silicon Detector Units (SDUs) arranged in three telescopes.
148 Measurements obtained with ALTEA are referred to the three orthogonal axes X, Y and Z
149 relative to the ISS: X is along the velocity vector, in the forward direction, being the axis of the
150 USLab and Russian modules; the truss is along the Y axis, as are the Columbus and JEM axes;
151 and +Z is directed towards the Earth, while -Z directed towards the zenith. During the
152 measurements described here, either all SDUs were used, assembled in a 3D structure (X, Y, Z

5

153   as shown in Figure 1) or only one (SDU2) was used, pointed along the Z axis. When used in the

154   3D configuration, the three axes of the detector are aligned with the three axes of the ISS.

155

156   Each SDU makes real-time measurements of the energy losses and trajectories of the particles

157   impinging on it, which may be primary cosmic ray ions or secondary particles produced in

158   interaction of primary particles with the ISS hull, shielding racks, etc.[1] NASA provides the

159   detailed orbital information needed to study the angular distribution of particle trajectories when

160   the ISS is flying in the three main geomagnetic zones (high latitude, low latitude, equator, and

161   SAA).

162

163   Each SDU consists of three pairs of silicon ladders; each pair is composed of two silicon chips

164   segmented in 32 strips with 2.5 mm pitch. Strip segmentation on each ladder is alternately

165   oriented along orthogonal directions to use the two strip coordinates and the height of the ladder

166   pair into the detector as the three coordinates in space. Each silicon chip has a size of 8 cm × 8

167   cm, and a thickness of 380 μm. The inter-planar space between a ladder pair is 3.75 mm, while

168   the distance between two pairs is 37.5 mm. This structure results in a geometrical factor of 230

169   cm^2 sr per single SDU. The Linear Energy Transfer (LET, in silicon) range of the detector goes

170   from a threshold of about 2.5 keV/μm up to about 800 keV/μm. Under certain conditions, the

171   charge of each impinging particle can be estimated (see Di Fino et al. 2012 for details).

172

173   The detector is triggered by fully penetrating particles that deposit energies above threshold on

174   all the odd planes of an SDU. Therefore, each SDU can measure protons with kinetic energies

175   from about 25 MeV to about 45 MeV, ^{4}He from about 25 MeV/n to about 250 MeV/n, and all

176   other penetrating particles up to relativistic molybdenum. Further details are given in Zaconte et

177   al. (2010). The data transfer from ISS to the ground is described in Di Fino et al. (2006).

178

---

[1] The trigger and nature of the detector does not allow discrimination between forward and backward moving particles. It is therefore appropriate to treat each telescope as double-ended for purposes of calculating the geometric factor.

179 2.2.1 Data Preparation and Selection

180 ALTEA data are first processed to subtract pedestals (ADC readings with zero input). Pedestal

181 data are obtained periodically throughout the measurements to track possible shifts. Events are

182 then selected in which only a single track is present. The energy deposits in the silicon planes

183 (ΔE) are adjusted to vertical incidence according to $\Delta E_{in} = \Delta E \cos (\theta_{in})$, where θ_{in} is the angle

184 between the direction of the incident particle and the normal to the silicon surface.

185

186 2.2.2 Analysis

187 We calculate the flux integrated over all ion types. Averaging periods of one day and one minute

188 are used. The latter data are important for resolving variations that arise from the ISS orbit,

189 specifically as the trajectory takes the spacecraft from high latitudes with low geomagnetic

190 cutoffs to low latitudes with high geomagnetic cutoffs, and through the South Atlantic Anomaly

191 a few times per day.

192

193 We bin the data according to different parts of the orbit: high latitude (hereafter *HL*), low latitude

194 (hereafter *LL*), or over the South Atlantic Anomaly (*SAA*). The selection criteria rely on the

195 magnetic coordinates L (the McIlwain parameter, with units of Earth radii) and B (McIlwain

196 1961), which are downloaded together with the geographical orbital coordinates. The following

197 definitions are used: *HL* corresponds to L > 3; *LL* corresponds to L < 1.5 and B > 0.27 G; the

198 *SAA* is defined as L < 2.4 & B ≤ 0.27 G). For ions with charge-to-mass ratios of one-half (e.g.,

199 carbon, nitrogen, oxygen, silicon, etc.), the *HL* vertical cutoff rigidity defined by L > 3

200 corresponds to kinetic energies less than about 300 MeV/nuc; the large majority of GCRs have

201 energies greater than this.

202

203 *2.3 CRaTER*

204 The Cosmic Ray Telescope for the Effects of Radiation (Spence et al. 2010), known as CRaTER,

205 is aboard the Lunar Reconnaissance Orbiter (LRO), which reached lunar orbit in July 2009.

206 LRO's orbit was circularized in September 2009, and CRaTER has been recording GCR and

207 SEP fluxes with very few interruptions since that time. CRaTER provides an almost continuous

208 measurement spanning the extremely deep Cycle 23 solar minimum, the ascending phase and

209 maximum of the anomalously weak Cycle 24, and the present (as of this writing) descending

210 phase of Cycle 24.

211

212 The design of the CRaTER instrument was described in detail by Spence et al. (2010). It is

213 unusual in that much of the volume of the six-element telescope is occupied by an inert material,

214 A-150 Tissue-Equivalent Plastic (TEP). The diodes are arranged in three pairs, each pair

215 consisting of one thin (148 μm) and one thick (1000 μm) planar silicon diode, as shown

216 schematically in Figure 2. The telescope's boresight is usually pointed towards the zenith, with

217 occasional brief exceptions when the spacecraft is rotated away from its nominal position for

218 purposes of imaging particular lunar features. The first detector pair (D1, D2) is under minimal

219 shielding and measures the free-space environment; a 6 g cm^{-2} piece of TEP separates the first

220 pair from the second (D3, D4), and a second piece of TEP, 3 g cm^{-2} in depth, separates the

221 second pair from the third (D5, D6). The thick detectors (D2, D4, D6) are sensitive to all charged

222 particles, but their pulse-height readout electronics saturate at an LET value (in silicon) of about

223 88 keV/μm. The thin detectors (D1, D3, D5) do not efficiently record particles with LET in

224 silicon below about 7 keV/μm, but can measure up to 2000 keV/μm. Therefore, to obtain a LET

225 spectrum over the full range relevant for dosimetry, it is necessary to combine the data from the

226 thin and thick detector in each pair. This is a non-trivial consideration due to the straggling of

227 high-energy particles in thin detectors (Bichsel 1988), which complicates efforts to match up

228 spectra from the thin and thick detector pairs (Case et al. 2013; Zeitlin et al. 2013). LET spectra

229 from the deep 2009-2010 solar minimum and weak solar maximum period of 2014-2015 are

230 available (Zeitlin et al. 2015).

231

232 In analyzing CRaTER data, it is necessary to impose a coincidence requirement of at least two

233 detectors (e.g., D2·D4) in order to filter the event sample to a reasonable size and to constrain the

234 path length distribution Different coincidence modes in CRaTER have different geometric

235 factors; in the analysis presented here, we select events that satisfy the D2·D4·D6 coincidence

236 criteria, in order to make use of the most-shielded detectors. The choice of coincidence imposes

237 a species-dependent lower limit on the incident energy of incoming particles, as explained in

238 detail by Case et al. (2013). For example, the minimum kinetic energy to obtain a D2·D4

239 coincidence is about 92 MeV for normally-incident protons; at the other extreme, for a ^{56}Fe ion

240 to satisfy the D2·D4·D6 coincidence condition requires an incident energy of at least 525

241 MeV/nuc (assuming the Fe does not undergo fragmentation in either piece of TEP). Other

242 relevant cases are somewhere between these extremes.

243

244 Geometric factors for the two most-employed coincidence requirements are given in Table 1.

245 The table also includes parameterized approximations for penetration energies and fragmentation

246 losses as functions of the charge Z of the incident ion. The quoted geometric factors are

247 simplified in that they do not include the effects of scattering or secondary production, nor do

248 they account for "out-of-cone" particles that may cause coincidence triggers via secondary

249 production. A detailed discussion of these effects can be found in Appendix B of Case et al.

250 (2013) and the Appendix to Zeitlin et al. (2013).

251

252 In the nominal orbit and nominal orientation, CRaTER is effectively a one-ended telescope, with

253 the large majority of particles entering from the zenith-pointing side of the telescope. Albedo

254 protons produced in the lunar surface are also observed (Wilson et al. 2012), but contribute less

255 than 10% of the dose (Spence et al. 2013) and can be removed from the data sample by

256 appropriate cuts. Albedo protons with high LET in D6 (as required in this analysis) do not have

257 sufficient energy to reach D2, which is required for the present analysis, so these particles do not

258 contribute.

259

260   Table 1: CRaTER Telescope Geometric Factors and Related Quantities

Coincidence	Nominal Geometric Factor, G (cm^2 sr)	Minimum Incident Energy (MeV/nuc)	Fraction Undergoing Nuclear Fragmentation
D2·D4	1.91	$70 \times Z^{0.52}$	$0.11 \times Z^{0.46}$ (TEP1)
D2·D4·D6	0.603	$87 \times Z^{0.53}$	$0.17 \times Z^{0.47}$ (TEP1+2)

261

262 ***2.4 MSL-RAD***

263 The Radiation Assessment Detector (RAD) is part of the Mars Science Laboratory (MSL)

264 science payload. The instrument is mounted on the top deck of the Curiosity rover, presently

265 exploring Gale Crater on Mars. The design and calibration of the RAD instrument are described

266 in detail by Hassler et al. (2012), and Zeitlin et al. (2016), respectively, and a schematic diagram

267 of RAD is shown in Figure 3. Results of the RAD observations obtained during the transit to

9

268 Mars are discussed by Zeitlin et al. (2013) and Kohler et al. (2016), and on the surface of Mars

269 by Hassler et al. (2014), Ehresmann et al. (2014), Rafkin et al. (2014), Kohler et al (2014), Guo

270 et al. (2015) and Wimmer-Schweingruber et al. (2015). RAD data can be used for dosimetry, to

271 distinguish charged particles from neutral particles, and to determine spectra in limited energy

272 ranges for all ions species from H to Fe, albeit with very limited statistical precision for the

273 heavier ions owing to the extremely compact size of the instrument. In the following analysis, we

274 will use data from the charged particle telescope comprised of the inner segment of the A diode

275 (referred to as the "A2" detector) and the B detector. The geometric factor for this coincidence

276 cone is 0.17 cm^2 sr when RAD is on the surface of Mars with charged particles coming almost

277 exclusively from above, and was 0.34 cm^2 sr during the cruise to Mars, when particles could

278 enter the telescope from either direction.

279

280 The MSL spacecraft, with Curiosity inside, was launched to Mars on November 26, 2011. RAD

281 was turned on for the first time on 6 December 2011, and operated almost continuously

282 throughout the cruise, until being switched off on 14 July 2012 in preparation for Curiosity's

283 landing. The data set obtained in this period was the first of its kind, and it is pertinent to

284 possible human missions to Mars or other destinations in deep space, presumably under roughly

285 similar shielding conditions. Data obtained by RAD in the deep-space radiation environment

286 allow many interesting points of comparison to data from ALTEA and CRaTER.

287

288 Dosimetric results published previously (Zeitlin et al. 2013; Hassler et al. 2014) were obtained

289 using RAD's onboard analysis of energy deposits in the B (silicon) and E (tissue-like plastic)

290 detectors. These are conceptually simple: whenever a hit above threshold is recorded in one of

291 these detectors, the energy deposit as calculated onboard from calibrated pulse-height data is

292 added to the running total for the current time increment. RAD operates on an "observation"

293 cycle, where the observation duration is an adjustable parameter that has typically been set to be

294 16 minutes. Within each observation, onboard data analysis software records B and E energy

295 deposits in 16 equal intervals (1 minute each with the 16-minute cadence). The total energy

296 deposited per time interval for both B and E is telemetered to Earth, where straightforward

297 methods are used to convert these data to dose rates in silicon and plastic, respectively.

298

10

299   The RAD dose rates described above, and previously reported in the literature, are

300   "omnidirectional," since all energy depositions contribute, regardless of the direction of travel of

301   the incident particle. This is in contrast to dose rates obtained with CRaTER and ALTEA, where

302   charged particle fluxes are measured in narrow cones, and the fluxes are extrapolated assuming

303   isotropy of the incident radiation. To make the comparisons as mutually consistent as possible,

304   here we use RAD charged particle data in the viewing cone defined by the A2·B coincidence. As

305   explained in Ref. 11, A2 is the inner segment of the top diode in the silicon stack, and B is a

306   similarly-sized segment of the middle diode of the stack. The double-ended geometric factor of

307   this cone is 0.34 cm^2 sr, as mentioned above, and LET can be measured in the range from 0.1 –

308   1000 keV/μm in silicon. Inside the MSL spacecraft during the cruise to Mars, the (nominally)

309   upward-pointing field of view (FOV) was shielded very unevenly by the descent vehicle and its

310   hydrazine fuel tanks, as well as by the parachute system. We will return to this point below, in

311   Section 3.2.

312

313   Curiosity is powered by a radioisotope thermoelectric generator (RTG), which emits a steady

314   background of low-energy neutrons and γ-rays. These contributions to dose rates in B and E

315   were measured prior to launch; the dominant effect was seen in the B detector, with a

316   contribution of approximately 84 μGy/day coming predominantly from secondary electrons in

317   the 1-10 MeV range. These are created by interactions of high-energy γ-rays emitted from the

318   RTG. Some of these interactions occurred in the descent vehicle located directly above RAD in

319   the MSL cruise configuration; the descent vehicle was jettisoned during the landing phase, and

320   this results in a smaller observed RTG background (estimated to be 67 μGy/day) during surface

321   operations. No significant energy deposits were seen in the E detector during the pre-launch test.

322   It is likely that the large majority of energy deposits in E from RTG γ-rays and neutrons are

323   below the detection threshold, which is set to about 6 MeV, and the electrons that are seen in the

324   B detector do not reach E because it is shielded by other detectors, with D above it and 1.2 g cm^{-2}

325   of plastic on all other sides. This mass prevents the secondary electrons from reaching the E

326   detector, making it effectively blind to the RTG background. In general, when considering LET

327   spectra in the coincidence data, the contributions from the RTG must be subtracted. But because

328   these are limited to low LET, and the present analysis considers only relatively high-LET

329   particles, no background subtraction is needed here.

11

330

3. The Deep Space Radiation Environment

The deep space radiation environment is specifically the environment outside the influence of the Earth's magnetic field (or any other body's magnetic field). Even though the Moon orbits through Earth's distant magnetotail around the time near its full phase, the terrestrial magnetic fields are so weak at those distances that GCR and SPE particles freely access the Moon's surface (Huang et al. 2009; Case et al. 2010); the entirety of the lunar orbit is deep space for our purposes. The deep-space energetic particle environment is simple compared to the complexity encountered in various Earth orbits, including LEO. In deep space, there are only two significant sources of energetic charged particles, GCRs and SPEs. We ignore the ACRs (anomalous cosmic rays), as their fluxes are small and their energies too low to contribute significantly to the radiation dose, and in any case they are not measurable by shielded detectors since any electrons around the nucleus are immediately stripped when the particle encounters the shield. Previously, detectors sent into deep space such as those on the Advanced Composition Explorer (ACE) (Stone et al. 1998), Ulysses (Simpson et al. 1992), and High Energy Astrophysical Observatory (HEAO) (Bouffard et al. 1982) were designed to measure differential flux distributions (dJ/dE) in the free-space (i.e., unshielded) environment. More recently, though, with future human missions into deep space being considered, CRaTER and RAD have traveled to lunar orbit and to Mars, respectively, with the explicit intention of measuring the deep-space environments under shielding.

350

3.1 CRaTER Shielding

The view cones associated with various CRaTER coincidence geometries are narrow, so that no primary GCRs or SEPs can enter from the rear of the telescope when LRO flies in its nominal orientation, in which the rear field of view is completely filled by the lunar disc. For particles in the telescope fields of view, the CRaTER detectors are shielded only by the TEP that is an integral part of the design, as described above. The middle detector pair sits under 6 g cm^{-2} of shielding, comparable to the depth of shielding over bone marrow in an astronaut, and the detector pair at the nadir end is under a total of 9 g cm^{-2}. Because CRaTER sits on the outside of the LRO spacecraft, this shielding depth can be compared to that experienced by an astronaut

360 during an extravehicular activity (EVA), either outside a spacecraft in deep space or perhaps

361 roving the lunar surface. Since we measure telescope fluxes in a narrow cone and extrapolate to

362 dose in larger angular ranges assuming isotropy, we are free to choose the extent of the

363 extrapolation.

364

365 It is important to note that the TEP shielding in CRaTER is designed to affect particles in the

366 telescope fields of view. Particles that enter from the side may pass through little or no TEP (or

367 through a considerable depth of TEP) before being detected. Since the CRaTER readout

368 electronics are configured to read out the full stack when any single detector is hit, it is possible

369 to use the data for simple dosimetry in a manner akin to the onboard, omnidirectional dosimetry

370 done by the RAD instrument (i.e., summing up the energy from all hits above threshold for a

371 given detector). However, dose readings obtained this way are dominated by particles coming

372 from outside the telescope FOV, which defeats the purpose of the instrument's design. It is

373 therefore essential, when analyzing CRaTER data, to impose either a two-fold coincidence

374 requirement using detectors separated by one TEP piece, or a three-fold coincidence that requires

375 that the stack be fully penetrated. These cuts, in turn, impose kinetic energy requirements on the

376 incident particles. For instance, requiring that an incident ^{56}Fe ion fully penetrates the stack

377 limits the measurable energy range to those ions with at least 525 MeV/nuc.

378

379 ***3.2 RAD Shielding in Cruise***

380 As mentioned above, the shielding around RAD during MSL's cruise to Mars was complex. A

381 significant fraction (roughly half) of the upward-pointing FOV was very lightly shielded. This

382 can be seen in Figure 4, which shows a polar plot based on a simplified mass model provided by

383 colleagues at the NASA Jet Propulsion Laboratory, where the MSL mission is managed. The plot

384 corresponds to the shielding of the upper hemisphere, i.e., for particles coming into RAD from

385 above. Because the detector segments are hexagonal in outline, the fields of view are not

386 perfectly circular, but for present purposes the A2·B cone can be considered to extend to angles

387 from 0° to 20°. In this range of polar angles, roughly half of the azimuthal angular range was

388 shielded by 5 g cm^{-2} or less. However, the other half of the azimuth contained highly varying

389 amounts of material, with many regions having more than 40 g cm^{-2} of shielding, and the most

390 heavily shielded regions having up to 80 g cm^{-2}.

13

391

392   It was also possible for energetic particles coming from the "backward" direction to fire the

393   A2·B coincidence. Particles from that direction had to penetrate the spacecraft heat shield ($\sim$ 1 g

394   cm^{-2}) the RAD Electronics Box ($\sim$ 5 g cm^{-2}) as well as the F, E, D, and C detectors to produce an

395   A2·B coincidence. Of these, the D detector provides by far the most shielding, 12.5 g cm^{-2} of

396   CsI, while the E and F together provide another $\sim$ 3 g cm^{-2}, for a total of about 22 g cm^{-2}. This

397   was more uniform than the shielding of the upper hemisphere.

398

399   ***3.3 RAD Shielding on Mars***

400   The Curiosity rover successfully touched down in Gale Crater on August 6, 2012. RAD and the

401   other science instruments, including the REMS weather station (Gómez-Elvira et al. 2012),

402   began taking data the next day. The REMS sensor suite includes an atmospheric pressure sensor

403   (Harri et al. 2014), which has proven to be an important tool for understanding RAD data. In

404   particular, diurnal variations are observed in the dose rate and neutron fluences measured by

405   RAD (Rafkin et al. 2014; Guo et al. 2015). The variations arise from the "thermal tide," which

406   results in relatively low atmospheric pressure on the day side of Mars and higher pressure on the

407   night side. The atmosphere above RAD, which consists almost entirely of CO_2, averages about

408   23 g cm^{-2} in depth for vertical rays. As the slant angle of particles coming through the

409   atmosphere increases, so too does the shielding depth, by a factor of $1/\cos(\theta)$ where θ in the

410   angle from the vertical. Particles incident at angles corresponding to the outer limit of the A2·B

411   viewing cone traverse an additional 6.4% depth of CO_2 ($\sim$ 1.3 g cm^{-2}) before reaching the

412   detector. The distribution of charged particles reaching RAD has been shown to be very nearly

413   isotropic within the coincidence cones (Wimmer-Schweingruber et al. 2015). Assuming isotropy,

414   the average angle of incidence is 9°; particles arriving at this average angle see only an additional

415   1.1% of CO_2 compared to those with exactly vertical trajectories. The pressure varies about ±7%

416   from the mean on each sol (Martian day), with the highest pressures coming in the early morning

417   hours when temperatures are lowest, and the lowest pressures in the late afternoon when the

418   temperature peaks. The diurnal variations of column depth are therefore about twice as

419   significant as variations in column depth that arise from the slant angle distribution for angles

420   within the A2·B FOV.

14

421

422   Above, we mentioned that in situations with highly anisotropic shielding, we do not expect that

423   the dose measured in a narrow angular cone (e.g., like the one defined by A2·B) is equal to that

424   corresponding to the full 2π or 4π geometry. That was the case for RAD in cruise, and it is also

425   true as it measures the radiation environment in Gale Crater, due to the fact that paths through

426   the atmosphere increase with slant angle. Therefore, we do not expect that the charged particle

427   dose rates obtained from A2·B coincidence data will necessarily match the omnidirectional dose

428   rate obtained using only the B or E detectors.

429

430   **4. The LEO Radiation Environment**

431   The ISS is in LEO, with altitudes typically in the 400-450 km range and a 51.6° inclination. The

432   shielding provided by Earth's magnetic field is a complicated function of heliospheric conditions

433   which vary over time, as well as the altitude, latitude, and longitude of orbiting spacecraft. The

434   geomagnetic field prevents relatively low-energy particles from reaching the altitudes of

435   spacecraft in LEO. The typical energy required for an incoming charged particle to reach LEO is

436   strongly dependent on the geomagnetic latitude, and is often described in terms of the vertical

437   cutoff rigidity or energy associated with a particular geomagnetic latitude (Smart & Shea 2005).

438   ISS geodetic latitudes vary between the equator and 51.6°, corresponding roughly to vertical

439   cutoff rigidities of ~ 14.5 GV (13.6 GeV kinetic energy for a proton) and ~ 0.4 GV (~ 100 MeV

440   proton kinetic energy) at 400 km altitude. Ions such as ^{4}He, with Z/A of 1/2 (compared to Z/A of

441   1 for protons) have larger rigidities for a given velocity, and therefore penetrate the magnetic

442   field more readily than protons. Calculated values of vertical cutoff rigidity should not be

443   interpreted as "hard" cutoffs; rather, as Smart and Shea (2005) described, "in most cases, the

444   transmission of charged particles decreases from fully allowed to totally forbidden over a

445   discrete and often surprisingly large range of charged particle rigidities." Thus, even at the

446   highest latitudes of the ISS orbit, the magnetic field provides some shielding, and at low latitudes

447   some particles with rigidities less than the vertical cutoff value may reach LEO. In general, it is

448   not possible to disentangle the effect of magnetic shielding from that of bulk shielding in the data

449   presented here. As mentioned above, in this analysis we use only ALTEA data acquired at high

450   magnetic latitudes, where the geomagnetic shielding is minimal.

451

4.1 Bulk Shielding

452 *4.1 Bulk Shielding*

453 The bulk shielding provided by various parts of the ISS such as the hull, equipment racks, etc., is

454 typically not known with great precision for any given location. Efforts to improve the situation

455 are ongoing, but it is also the case that the shielding of a given location within the ISS varies

456 over time, as new items arrive, and other items already aboard are shifted to new locations or

457 returned to Earth.

458

459 *4.2 Geomagnetic Shielding*

460 From the standpoint of radiation protection, bulk shielding and geomagnetic shielding are

461 functionally similar: both screen out lower-energy particles but allow high-energy particles to

462 pass through. Nuclear interactions occur in bulk shielding, producing secondary particles,

463 whereas magnetic shielding entirely screens out lower-energy particles with no secondary

464 production. Since ions heavier than protons generally have A/Z ratios of 2 (or close), they are

465 more able to penetrate a magnetic field for a given ion velocity. This differential screening

466 should in principle be observable as a function of geomagnetic latitude in measurements made by

467 an unshielded detector in LEO such as AMS-02 (Caaus 2009). That is, the ratio of ions with Z >

468 1 to protons is expected to be higher in LEO than it is in deep space. However, to some extent,

469 the considerable bulk shielding on the ISS shifts the ratio back in the other direction, since the

470 fluxes of heavier ions are depleted by fragmentation reactions and proton fluxes are increased by

471 these same reactions, as well as by inelastic reactions of high-energy protons as they traverse the

472 spacecraft's hull and interior materials.

473

5. Measurement Comparisons: Detector Capabilities and Available Data

474 **5.   Measurement Comparisons: Detector Capabilities and Available Data**

475 Comparisons between ALTEA, RAD, and CRaTER are shown below for solar quiet times

476 during most of 2012, when all were operating more or less continuously. RAD began operations

477 in December 2011 and was on almost constantly until a three-week shutdown that started 14 July

478 2012, just prior to Curiosity's landing on Mars. CRaTER operated continuously. ALTEA was

479 also mostly operational in this period, being stationed in the USLab module until June 7, 2012

480 (day of year 159), at which time it was moved to the Columbus module, where operations

481 resumed June 8 (day 160) and continued until November 15 (day 320). Clear differences are seen

482 in the measurements obtained in the two ISS locations. After Curiosity was successfully landed
483 on Mars, RAD operations resumed on August 6 (day 219), under substantially different shielding
484 conditions, providing another point of comparison. As we will show in the following, the free-
485 space GCR environment varied only modestly throughout 2012. Several coronal mass ejections
486 strengthened the interplanetary magnetic field and suppressed GCR fluxes throughout the course
487 of the year.
488
489 Because of its high trigger threshold, ALTEA detects only a small fraction of the protons and
490 helium ions that reach it, but it is highly efficient for incident heavy ions. The protons and
491 helium ALTEA detects are a mixture of primary GCRs and secondaries produced in shielding.
492 Heavy ions are rare: even at solar minimum, the flux of heavy ions ($Z > 2$) when integrated over
493 charge and energy is on the order of 5×10^{-3} pfu in free space (Zeitlin et al. 2015), and may be
494 significantly less behind shielding.
495
496 Both RAD and CRaTER have small geometric factors compared to that of ALTEA, by about two
497 orders of magnitude, and therefore collect far fewer high-LET events per unit time. To put this in
498 perspective, consider that with a geometric factor on the order of 1 and an integral flux on the
499 order of 10^{-3} pfu, the heavy ion count rate is less than 100 per day integrated over all species.
500 Adding to the complexities of direct comparisons between instruments, for most of the cruise
501 phase, RAD had an incorrect firmware setting which caused it to fail to store heavy ion pulse
502 height event records. These events were registered in various counters, and were included in the
503 onboard dosimetry calculation, but were not stored for telemetry to Earth. The configuration
504 error was corrected in the final month of cruise, and analysis of counter data, presented in detail
505 below, indicates that the fraction of charged particle events due to heavy ions did not undergo
506 much variation throughout cruise.
507
508 The minimum LET that can be measured by ALTEA, about 2.5 keV/μm in silicon, can be
509 reproduced in RAD and CRaTER data simply by making cuts in the respective dE/dx spectra. In
510 RAD, the detectors are 300 μm thick, so the corresponding energy deposition cut is at 900 keV.
511 The method used to obtain previously-published LET spectra [29, 30] has been modified slightly
512 to improve the estimation of the RTG-induced background, but this change has no effect when

17

513 we restrict the data to the high-LET range covered by the ALTEA data. LET spectra from
514 CRaTER were published (Zeitlin et al. 2015) for time periods representing the deep solar
515 minimum of 2009-2010 and the weak solar maximum of 2014-2015. The same methodology
516 used to obtain those spectra is used here, but in 2012, solar modulation was in between minimum
517 and maximum, and those results have not previously been published. The spectrum acquired in
518 the D5/D6 detector pair, shielded by 9 g cm^{-2} of tissue-equivalent plastic, is used here to examine
519 the region above 2.5 keV/μm in silicon. For the ALTEA and RAD data obtained in 2012,
520 shielding conditions varied, but CRaTER shielding was constant, which allows us to evaluate the
521 effects of solar modulation on the high-LET portion of the spectrum during the course of the
522 year.

523

524 In the following, we will use the average radiation quality factor, <Q>, as a convenient metric for
525 comparing heavy-ion spectra obtained by the three instruments. We use the ICRP 60 formulation
526 of <Q> for a mixed charged-particle radiation field (ICRP 1991), but doing so requires
527 conversion of the dE/dx spectra measured in silicon to approximate LET spectra in water. For
528 RAD and CRaTER data, we have simply applied a constant scale factor of 1.79, which
529 corresponds to a dose conversion factor of 1.30. (That is, to obtain dose in water from measured
530 dose in silicon, we would multiply by 1.30 in this method.) The conversion factor is an
531 approximation, described in detail in the Appendix of Schwadron et al. (2012). ALTEA
532 measurements of dE/dx in silicon were converted to LET in water using a method provided by
533 Benton et al. (2010), based on functional fits to the Bethe-Bloch equation. Because this analysis
534 uses only the high-LET portion of the spectrum, the <Q> values reported here are not directly
535 comparable to the much smaller values obtained by integrating over full LET spectra.

536

537 The flux, dose, and dose equivalent results below include the contributions from virtually all
538 GCR heavy ions with charge Z > 2. The minimum LET of 2.5 keV/μm in silicon eliminates
539 much, but not all, of the flux of GCR protons and helium, and relatively slow secondary protons
540 and helium ions produced in nuclear interactions can also pass this cut. The cut corresponds to a
541 maximum kinetic energy of about 250 MeV/nuc for ^{4}He and 36 MeV for protons. Among
542 primary GCRs, protons and helium ions are far more abundant than heavy ions, so even though
543 only small fractions of the fluxes of these ions have LET above the ALTEA threshold, their

544 contributions are significant in this analysis. Furthermore, in thickly shielded environments, low-
545 energy secondary protons and helium ions that have LET above the threshold are also abundant.
546 A simple simulation in a beam-like geometry was performed using the PHITS Monte Carlo
547 package (Iwase et al. 2002) for transport with an input spectrum derived from the 2014 version
548 of the Badhwar-O'Neill GCR model (Golge et al. 2014). A 20 g cm^{-2} aluminum shield was
549 simulated, probably similar to the average bulk shielding on ISS and comparable to the shielding
550 of RAD in Gale Crater. We find that low-energy protons and helium ions dominate the simulated
551 LET spectrum in the range from 3 to 10 keV/μm in silicon.

552

553 **6. Results, Part 1: Variations of Galactic Cosmic Rays in 2012**
554 The ALTEA data from 2012 are divided into two periods, days 1-159 (USLab) and 160-320
555 (Columbus module). For purposes of comparing to deep-space measurements, it is important to
556 understand the variations in the GCR flux in the inner heliosphere, which was affected by solar
557 activity over this time range. Days when the LET data were directly affected by the presence of
558 SEPs have been excluded in this analysis. CRaTER data are available for both of the ALTEA
559 measurement periods. The heavy-ion event storage problem described above makes it impossible
560 to construct the full LET spectrum for RAD data during period 1, but as there were not major
561 variations in the GCR flux during MSL's cruise to Mars, the data from late in cruise are likely
562 representative of the entire cruise, arguably with a very small upward correction, as discussed
563 below. The usable cruise data for creating a full LET spectrum are from the period from 12 June
564 to 14 July 2012 (days 164-196). Surface data for the first 100 Martian sols cover the second
565 measurement period, when ALTEA was in the Columbus module. Our goal in this section is to
566 assess the effects of modulation, facilitating both (1) the comparison of the first and second
567 ALTEA periods (days 1-159 vs. days 160-320), and (2) the comparison of the late-cruise RAD
568 data (days 164-196) vs. the earlier ALTEA period (days 1-159).

569

570 To address the first of these points, in Figure 5 we show CRaTER data (black data points) that
571 represent our best estimate of the integral flux of ions with LET above 2.5 keV/μm in silicon, for
572 the most-shielded detector pair (9 g cm^{-2}). The increasing solar activity through 2012,
573 particularly the first half of the year, led to a decreasing flux of these ions, from about 0.017 pfu
574 at the start of the year to about 0.013 pfu by day 320. Averaging over the two periods defined by

575   ALTEA locations, we find that the high-LET GCR flux was 15% lower in the later period. We

576   can also use these data to compare days 164-196 to days 1-159; we find a 2% decrease in the

577   later period.

578

579   A second measure of modulation affecting the late-cruise RAD data can be derived from RAD

580   count-rate data. RAD has a dedicated trigger that fires on coincidences of high-LET hits in the

581   A2 and B detectors. The threshold for this trigger was set incorrectly at launch, but was raised to

582   a suitable level of about 2.4 MeV on January 27, 2012. At this time, a SEP event was in progress,

583   and its effects lasted for several days; the count rate stabilized on day 32. The threshold on this

584   trigger corresponds to a dE/dx in silicon of about 8 keV/μm, significantly higher than the 2.5

585   keV/μm used in the rest of this analysis, but the count rate is nonetheless useful. For days 32-

586   159, the average high-LET flux recorded by this counter was $(1.03 \pm 0.01) \times 10^{-2}$ pfu, and from

587   days 164-196, $(0.99 \pm 0.02) \times 10^{-2}$ pfu, a decrease of $4 \pm 2\%$. This is compatible, within

588   uncertainties, with the 2% decrease seen in the CRaTER data (to which a lower threshold cut

589   was applied). The flux derived from the heavy-ion trigger rate is plotted in red in Figure 5. Data

590   obtained after landing (day 220 *et seq*.) are included in the plot. Cruise data were normalized

591   using the double-ended geometric factor, whereas surface data were normalized using the single-

592   ended geometric factor. The RAD heavy ion trigger measured a lower flux during cruise than

593   was measured with CRaTER during the same period due to the higher threshold in the RAD

594   data; the RAD rate dropped further after landing, due to additional shielding provided by the

595   Martian atmosphere. Note that, in cruise, the count rate for the RAD heavy-ion trigger with the 8

596   keV/μm threshold was about 1.1% as large as the count rate for the trigger that fired on low-LET

597   charged particles, consistent with the observation that heavy ions make up about 1% of the GCR

598   flux in free space. This percentage dropped to 0.5% in the surface data.

599

600   Additional information about changes in the GCR flux from early 2012 to mid-2012 comes from

601   comparing the LET spectrum obtained with CRaTER for the period from January 1 to January

602   22 (just before the first large SEP events of the year) to that obtained during the same June 12 –

603   July 14 period used in the analysis of RAD data. In the intervening months, five SEP events

604   occurred, which slightly suppressed the GCR flux as illustrated in the preceding. Using CRaTER

605   spectra to compare the two periods in terms of average LET, we find a statistically-insignificant

606 difference of about 0.8%. We conclude that the main effect of the increased modulation that

607 followed the five SEP events in the first half of 2012 was to reduce the overall intensity of the

608 GCR, without causing any major shifts in the LET spectrum. This finding is consistent with

609 earlier work [25], in which it was determined that, at 9 g cm^{-2} shielding depth, LET spectra at

610 solar minimum and maximum have very similar shapes and differ mainly in the total fluxes of

611 ions populating the spectra.

612

7. Results, Part 2: LET Spectra Comparisons

614 *7.1 Period 1*

615 In the first two rows of Table 2, we show dosimetric quantities for days 1-159 for ALTEA and

616 CRaTER, for LET > 2.5 keV/μm. The third row shows RAD cruise results for days 164-196, to

617 which a 3% upward correction has been applied to the flux to at least approximately compensate

618 for the increased solar modulation relative to the average for the day 1-159 period. This

619 correction is based on the mutually-consistent estimates from the CRaTER data (2%) and from

620 the RAD heavy-ion trigger count rate (4 ± 2%). The notation "2π Dose Rate" refers to the

621 normalization chosen for all data sets − we have in all cases extrapolated from the fluxes

622 measured in limited-angle telescope geometries to a 2π geometry, corresponding to an isotropic

623 distribution of the incident particles coming from one hemisphere. This represents, to a good

624 approximation, the situation in LEO for a zenith-pointing telescope, in lunar orbit or on the

625 surface of the Moon, and on the surface of Mars. It is also our motivation for choosing ALTEA

626 results from the Z-axis SDU for the comparison during the first period, since this SDU pointed

627 zenith/nadir. The RAD cruise data were taken in interplanetary space, where the more

628 appropriate extrapolation would be to 4π geometry, but we have opted to maintain a consistent

629 normalization among all data sets. The LET spectra are shown in Figure 6.

630

631 The uncertainties assigned to the <Q> values reported here represent the statistical and

632 systematic errors for all instruments, which have been combined by adding them in quadrature.

633 For all the spectra used in this analysis, we find that the result for <Q> is sensitive at about the

634 3% level to reasonable variations in the method of scaling LET in silicon to LET in water. For

21

635 ALTEA and CRaTER, this is the dominant uncertainty; for RAD, the combined uncertainty is
636 dominated by statistics.

637

638 Binning of the LET spectra is different for the different instruments. RAD pulse-height data are
639 telemetered to Earth after the onboard processing software performs logarithmic compression of
640 the deposited energy scale, hence the binning of RAD data is inherently logarithmic. For
641 CRaTER data, to obtain reasonable statistics at all LET values, we have used bins that are 1
642 keV/μm wide up for LET's up to 100 keV/μm, 4 keV/μm wide from 100 to 300 keV/μm, and 10
643 keV/μm wide above 300 keV/μm. ALTEA data have bin widths of 1 keV/μm across the entire
644 spectrum.

645

646 Table 2 – Average Dosimetric Quantities (SEP Periods Excluded), LET > 2.5 keV/μm, 2012
647 Days 1-159

Instrument	Day of Year (2012)	Flux (10^{-3} pfu)	2π Dose Rate in H_2O (nGy/sec)	<Q> (ICRP 60)	DoseEquivalent Rate (nSv/sec)
ALTEA (High latitudes only, USLab, Z-axis)	1-159	10.4	0.42	5.1 ± 0.2	2.1
CRaTER (D5-D6)	1-159	15.7	1.10	7.0 ± 0.2	7.6
RAD (cruise, adjusted)	164-196	17.5	0.89	7.0 ± 0.4	6.3

648

649 The adjusted results from RAD cruise data and CRaTER for days 1-159 shown in Table 2 are
650 quite similar, consistent with the similarity of the spectra shown in Figure 6. Both detectors
651 measured considerably larger fluxes, dose rates, and dose equivalent rates than ALTEA did for
652 the same period. The similarity of RAD and CRaTER results is, on first glance, somewhat
653 surprising since the two detectors were under dissimilar shielding: CRaTER results are obtained
654 under 9 g cm^{-2} of TEP shielding, while RAD was under highly inhomogeneous shielding that
655 averaged about 16 g cm^{-2} in the A2·B FOV. The fact that complex shielding produces a high-
656 LET spectrum similar to that measured under a much smaller depth of TEP is likely due to the
657 inhomogeneity of the shielding around RAD: a high percentage (roughly 25%) of paths in the
658 A2·B FOV were shielded by less than 5 g cm^{-2} of material. These lightly shielded paths allowed
659 heavy ions to reach RAD with a high probability of surviving without first undergoing
660 fragmentation into lighter ions. The median (as opposed to mean) shielding depth in the RAD
661 FOV was very close to 9 g cm^{-2}, which is also the depth of shielding used to obtain the CRaTER

662   result; this suggests that the median shielding depth may be a more robust index of shielding than

663   the mean depth when shielding is highly variable. The RAD and CRaTER fluxes for high-LET

664   particles are both substantially greater than those found by ALTEA at high latitudes.

665

666   In Figure 6, over much of the spectrum, the fluxes measured by ALTEA are a factor of 1.5 to 2

667   below those measured in deep space. In the range from about 50 to 200 keV/μm, differences are

668   factors of 2.5 to 5, and at higher LET, differences are somewhat smaller. The integral fluxes are

669   dominated by the LET bins with the highest fluxes, i.e., those below ~ 20 keV/μm, where the

670   differences are less pronounced, hence the overall difference of a factor of ~ 1.5 in Table 2.

671

672   *7.2 Period 2*

673   Figure 7 and Table 3 show results for period 2, after ALTEA was moved to the Columbus

674   module, where it was evidently under much less shielding than it was in the USLab. The RAD

675   data for this period were obtained on the Martian surface. RAD and CRaTER again measured

676   larger fluxes and doses than did ALTEA, but in period 2, the differences between RAD and

677   CRaTER are significant, whereas they were much smaller in period 1. This is almost certainly

678   due to the increased shielding RAD is under on the surface of Mars compared to cruise. For this

679   later period, the average Q value measured by ALTEA is the largest of any of the values reported

680   here, whereas the RAD surface result is similar to that obtained by ALTEA when it was

681   positioned in the USLab. The large <Q> measured by ALTEA in Columbus drives the dose

682   equivalent rate to a value greater than that measured by RAD on Mars, but still significantly less

683   than that measured by CRaTER in the same time period.

684

685   Table 3 – Average Dosimetric Quantities (SEP Periods Excluded), LET > 2.5 keV/μm, 2012

686   Days 160-320

Instrument	Day of Year (2012)	Flux (10^{-3} pfu)	2π Dose Rate in H_2O (nGy/sec)	<Q> (ICRP 60)	DoseEquivalent Rate (nSv/sec)
ALTEA (High latitudes only, Columbus, Z-axis)	160-320	9.2	0.53	8.2 ± 0.3	4.4
CRaTER (D5-D6)	160-320	13.6	0.97	7.1 ± 0.2	6.8
RAD (surface)	220-320	13.2	0.56	5.6 ± 0.3	3.1

687

688   In Figure 7, it can be seen that the fluxes measured by ALTEA in the Columbus module are
689   significantly closer to the CRaTER fluxes than were the fluxes measured by ALTEA in the
690   USLab. Below 100 keV/μm, the fluxes measured by all three instruments are very similar.
691   Above 100 keV/μm, ALTEA and CRaTER measured very similar fluxes, while RAD fluxes are
692   systematically smaller than those from the other two detectors.
693

694   A considerable amount of evidence, including the CRaTER results for the two periods as shown
695   in Tables 2 and 3, suggests that the average GCR flux in the inner heliosphere was about 10% to
696   15% less in the later period 2. The flux measured by ALTEA dropped by about 10% from period
697   1 to 2, as a result of some combination of increased modulation and reduced bulk shielding. Yet,
698   despite the greater solar modulation and the corresponding decrease of the primary GCR flux,
699   ALTEA measured higher dose and dose equivalent rates in the later period, and measured a
700   much larger <Q>. The obvious conclusion is that the bulk shielding in the USLab was
701   substantially greater than in Columbus, and greatly attenuated the heavy ion flux. The USLab
702   shielding was also apparently greater than the atmospheric shielding above RAD on Mars. This
703   deep shielding and consequent secondary production in the USLab may explain the ~ 10% larger
704   flux as measured by ALTEA in that location compared to the flux measured in Columbus; a self-
705   consistent explanation is that, in the USLab, ALTEA saw a relatively large share of low-energy
706   secondary protons and helium, which drove up the flux while driving down <Q>. Careful
707   examination of the LET data confirms this: the flux in period 2 is higher than in period 1 except
708   at the very lowest LET's measured, but, as mentioned, the low-LET portion of the spectrum
709   dominates the integral.
710

711   *7.3 General Observations*
712   For both periods, fluxes and dose rates were smaller in ALTEA than in the RAD and CRaTER
713   deep-space measurements. At lower geomagnetic latitudes, the differences between LEO and
714   deep-space spectra are even greater. In the USLab, the dose equivalent rate compared to that of
715   CRaTER was smaller by a factor of 3.6. When ALTEA was in a less-shielded location in the
716   Columbus module, the factor was only 1.5 compared to CRaTER, and was greater than the rate
717   measured by RAD on Mars. Again, these differences are attributable to the heavy bulk shielding

718   in the USLab. It is notable that in all cases, the <Q> values agree to within about ±20% of the

719   average (with all instruments weighted equally), and the LET distributions have similar shapes.

720

721   It is informative to compare the dose and dose equivalent rates for RAD shown in Tables 2 and 3

722   with results obtained by integrating over the entire LET spectrum. The results shown here differ

723   from previously-reported results in that they are obtained by extrapolation of the telescope

724   results to 2π, rather than using omnidirectional data as was done previously. Extrapolating the

725   telescope results from the cruise data to a 4π geometry yields a tissue dose rate of 3.9 nGy/sec

726   and a dose equivalent rate of 14.1 nSv/sec; these rates are about 25% less than the corresponding

727   published omnidirectional rates. About 41% of the dose and 84% of the dose equivalent come

728   from particles above the 2.5 keV/μm threshold. The dose share is highly consistent with results

729   reported earlier in comparison of ALTEA data with data from the DOSTEL instrument (Narici et

730   al., 2017). In contrast to the cruise results, when RAD surface data are integrated over the entire

731   LET spectrum, using an extrapolation to 2π, the dose rate is found to be 3.2 nGy/sec, about 30%

732   greater than the omnidirectional rate. The dose equivalent rate using this method is found to be

733   8.9 nSv/sec. The high-LET results in Table 2 correspond to 33% and 75% of the dose and dose

734   equivalent, respectively, for the surface data.

735

736   The fact that the extrapolated telescope dose rate was smaller than the omnidirectional dose rate

737   during cruise suggests that the telescope FOV was more heavily shielded than the rest of the

738   solid angle as seen by RAD. This is not surprising in view of the fact that the descent vehicle and

739   associated fuel tanks were directly above RAD. On the surface, the telescope dose rate is larger

740   than the omnidirectional, which is explained by the fact that the telescope FOV, which is nearly

741   vertical, is the most thinly-shielded portion of the solid angle since atmospheric shielding depth

742   increases with the inverse of the cosine of the slant angle.

743

744   As a further check of our discussion above regarding the differences in solar modulation in the

745   two measurement periods, in Figure 8 we show the CRaTER LET spectra from the two periods,

746   here using a logarithmic scale for LET in order to facilitate the comparison at the low end of the

747   range. As expected, the shapes of the distributions are nearly identical to one another, and the

748 differences are small, with a roughly 15% decrease in the integral flux in the second
749 measurement period as compared to the first.
750

751   **8. Conclusions and Discussion**
752 Understanding the information coming from different radiation detectors positioned in different
753 spots in the solar system (inside and outside a vessel, in the geomagnetic field, in deep space, on
754 a planetary surface) provides useful tools to improve radiation countermeasure strategies. To
755 make best use of the results from all the area detectors in the ISS it would be necessary to have,
756 for each new detector, an initial comparison campaign with a co-located reference detector to
757 provide definitive cross calibration in the same environmental conditions, as recently described
758 by Narici et al. (2017). Work along these lines is in progress.
759

760 In this paper, we have endeavored to explain most of the differences found when comparing LET
761 spectra obtained inside the ISS to spectra obtained in deep space and on Mars. This is highly
762 relevant for possible future use of the ISS as a platform for performing radiation biology
763 experiments that could help refine estimates of the health risks to humans on deep-space
764 missions. The most important sources of discrepancies in the data reported here are: i) the
765 differences in triggering of the detectors, leading to different available LET windows, and ii)
766 bulk shielding in the field of view of each detector. While the effects of the triggering differences
767 can be described semi-quantitatively, the shielding differences are far more difficult to deal with,
768 especially when significant changes may occur due to the often-undocumented movements of
769 items aboard an inhabited vehicle like the ISS. Nevertheless, we confirm the expected result that
770 the shielding differences are of overwhelming importance when studying the energetic particle
771 radiation environment. This is well-known, but has not previously been experimentally
772 quantified; these measurements are the first attempt to do so.
773

774 It may be that we will have a similarly poor knowledge of the movements of massive objects
775 around the inside of future deep space vessels. In that scenario, the variability of the amount of
776 shielding will make area radiation monitoring less usable for risk assessment than it would be in
777 a more stable situation. On the other hand, the large differences that can be obtained by moving
778 equipment and other materials could be used to tailor shielding to the day-to-day and/or

26

779 emergency needs, contributing to a dynamic approach to radiation countermeasures and risk
780 mitigation. This will require real-time knowledge of the position and shielding efficiency of each
781 relevant piece of material, perhaps driven by a system of tagging and autonomous reporting
782 (Fink et al. 2017). In a scenario where shielding is well-known, and modifications are tracked in
783 real time, area monitoring would be particularly useful for validation of radiation transport
784 modeling.

785

786 The shapes of the LET spectra at all measurement locations considered here are remarkably
787 consistent. It is also notable that the average dose equivalent rate measured on ISS by DOSTEL
788 in the Columbus module was 0.65 mSv/day (Berger et al. 2016), compared to 0.64 ± 0.12
789 mSv/day on Mars reported by Hassler et al. (2014), although both sets of measurements are
790 highly variable with time, both short- and long-term. The ISS measurements include
791 contributions from passages through the South Atlantic Anomaly (SAA) which are dominated by
792 low-LET particles (protons and electrons); thus an ISS LET spectrum obtained over many orbits
793 and without regard to latitude would be significantly different than the ALTEA high-latitude
794 spectra shown here. When considering the ISS radiation environment over the full orbit, we must
795 take into account two major differences: i) the sharper spectra of the radiation reaching the ISS at
796 low latitudes due to geomagnetic screening of lower-energy ions, and ii) the contributions of
797 trapped particles in the SAA. Geomagnetic screening reduces the particle populations in the LET
798 spectra between the ion peaks (making the spectra 'sharper'), as was shown by Narici et al.
799 (2015). The SAA passes produce increases for LET < 10 keV/µm, and contribute a dose that
800 approximately compensates for the reduction in GCR dose caused by geomagnetic shielding.
801 Finally, high-LET data acquired inside the MSL spacecraft during its transit to Mars under
802 complex and highly inhomogeneous shielding are found to be similar to those acquired in lunar
803 orbit under 9 g cm^{-2} of TEP shielding.

804

805 For the purposed of conducting radiation biology experiments, the results from ALTEA obtained
806 at high geomagnetic latitudes in the USLab (where it was under heavy shielding) are, in the high-
807 LET range studied here, similar to those from RAD on Mars. This suggests that the heavily-
808 shielded regions of the ISS may provide a useful platform for studying the effects of long-
809 duration exposure to low-intensity, high-LET radiation on biological systems. Of course,

810 considering the ISS radiation environment over the whole orbit significantly dilutes this
811 similarity, as geomagnetic shielding at lower latitudes substantially reduces the intensity of the
812 environment inside ISS. Similarly, the high-LET radiation environment experienced by RAD en
813 route to Mars is comparable to that obtained on ISS at high latitudes in a relatively lightly-
814 shielded module such as Columbus. Again, though, one must consider the dilution of this effect
815 that would be found were all latitudes considered in the ISS data. Although the ISS radiation
816 environment is an imperfect proxy for either the lunar or Martian radiation environments, it is
817 nonetheless orders of magnitude closer than the widely-accepted radiation analogues provided by
818 the terrestrial particle accelerators that are used for most space radiobiology studies.

819

820 It is important to note that we have focused on GCR data from a time when solar cycle 24 was
821 approaching maximum. We need to validate these observations with additional data at other
822 times in the solar cycle. Solar minimum data would also be extremely valuable, and may be
823 available in the near future – RAD continues to operate on Mars as the solar cycle heads towards
824 minimum, and current plans call for an upgraded version of ALTEA to fly on ISS in 2019.
825 Further insights may be gleaned from comparing observations of the six solar particle events that
826 occurred while RAD was in transit to Mars and ALTEA was operating on the ISS.

827

840 **References**

841 Benton, E.R., E.V. Benton, and A.L. Frank. Conversion between different forms of LET. *Radiat.*
842 *Meas.*, **45**, 957-959, 2010, DOI: 10.1016/j.radmeas.2010.05.008.

843 Berger, T., Przybyla, B., Matthiä, D., Reitz, G., Burmeister, S., et al. DOSIS & DOSIS 3D: long-
844 term dose monitoring onboard the Columbus Laboratory of the International Space Station (ISS).
845 *J. Space Weather Space Clim.*, **6**, A39, 2016, https://doi.org/10.1051/swsc/2016034.

846 Bichsel, H. Straggling in thin silicon detectors. *Rev. Mod. Phys.* **60**, 663, 1988, DOI:
847 10.1103/RevModPhys.60.663.

848 Bouffard, M., J. J. Engelmann, L. Koch, A. Soutoul, N. Lund, B. Peters, and I. L. Rasmussen.
849 The HEAO-3 cosmic ray isotope spectrometer. *Astrophysics and Space Science*, **84**, 3-33, 1982.

850 Case, A.W., H.E. Spence, M.J. Golightly, J.C. Kasper, J. Blake, J. Mazur, L. Townsend, and C.
851 Zeitlin, GCR Access to the Moon as Measured by the CRaTER Instrument on LRO. *Geophys.*
852 *Rev. Lett.*, **37**, 2010, DOI:10.1029/2010GL045118.

853 Case, A.W., J.C. Kasper, H.E. Spence, C.J. Zeitlin, M.D. Looper, et al., "The deep space galactic
854 cosmic ray lineal energy spectrum at solar minimum," *Space Weather* **11**, 361-368, 2013,
855 DOI:10.1002/swe.20051.

856 Casaus, J. "The AMS-02 experiment on the ISS." In *Journal of Physics: Conference Series*, vol.
857 171, no. 1, p. 012045. IOP Publishing, 2009.

858 Cucinotta, F.A., H. Wu, M.R. Shavers, and K. George. Radiation dosimetry and biophysical
859 models of space radiation effects. *Gravitational and Space Biology* **16**, 11-18, 2003.

860 Cucinotta, F.A., M.Y. Kim, and L. Chappell. Space radiation cancer risk projections and
861 uncertainties-2012. NASA TP 2013–217375, 2013.

862 Curtis, S.B., and M.C. Wilkinson. Study of Radiation Hazards to Man on Extended Missions.
863 No. N--68-22849; NASA-CR--1037. Boeing Co., Seattle, Wash., 1968.

864   Di Fino, L., F. Belli, V. Bidoli, M. Casolino, L. Narici, et al. ALTEA data handling. *Adv. Space*
865   *Res.*, **37**, 1710–1715, 2006, DOI: 10.1016/j.asr.2005.01.105.

866   Di Fino, L., M.Casolino, C.De Santis, M. Larosa, C. La Tessa, L. Narici, P. Picozza, and V.
867   Zaconte. Heavy ions anisotropy measured by ALTEA in the International Space Station. *Radiat.*
868   *Res.* **176,** 397-406, 2011, DOI:10.1667/RR2179.1

869   Di Fino, L., V. Zaconte, A. Ciccotelli, M. Larosa, and L. Narici. Fast Probabilistic Particle
870   Identification algorithm using silicon strip detectors. *Adv. Space Res.*, **50**, 408, 2012, DOI:
871   10.1016/j.asr.2012.04.015.

872   Durante, M., and F.A. Cucinotta. Heavy ion carcinogenesis and human space exploration. *Nature*
873   *Reviews Cancer* **8**, 465-472, 2008, DOI: 10.1038/nrc2391

874   Durante, M., and F.A. Cucinotta. Physical basis of radiation protection in space travel. *Reviews*
875   *of Modern Physics* **83**, 1245-1281, 2011, DOI: 10.1103/RevModPhys.83.1245

876   Dye, D.L., and M. Wilkinson. Radiation hazards in space. *Science* **147**, 19-25, 1965, DOI:
877   10.1126/science.147.3653.19

878   English, R.A., R.E. Benson, J.V. Bailey, and C.M. Barnes. Apollo experience report: Protection
879   against radiation. NASA TN D-7080 (1973)

880   Ehresmann, B., C. Zeitlin, D.M. Hassler, R.F. Wimmer-Schweingruber, E. Böhm, et al. Charged
881   particle spectra obtained with the Mars Science Laboratory Radiation Assessment Detector
882   (MSL/RAD) on the surface of Mars. *J. Geophys. Res. - Planet*, **119**, 468-479, 2014, DOI:
883   10.1002/2013JE004547

884   Fink, P.W., T.F. Kennedy, L. Rodriguez, J.L. Broyan, P.H. Ngo, et al. Autonomous Logistics
885   Management Systems for Exploration Missions. Presented at AIAA Space and Astronautics
886   Forum and Exposition, Orlando, FL, 2017.

887   Golge, S., P.M. O'Neill, and T.C. Slaba. NASA galactic cosmic radiation environment model:
888   Badhwar-O'Neill (2014). *Proceedings of the 34th International Cosmic Ray Conference*
889   *(ICRC2015)*. 30 July - 6 August, 2015. The Hague, The Netherlands.

890 Gómez-Elvira, J., C. Armiens, L. Castañer, M. Domínguez, M. Genzer, et al. REMS: The
891 environmental sensor suite for the Mars Science Laboratory rover. *Space Sci. Rev.* **170**, 583-640,
892 2012, DOI: 10:1007/s11214-012-9921-1.

893 Guo, J., C. Zeitlin, R.F. Wimmer-Schweingruber, S. Rafkin, D. Hassler, et al. Modeling the
894 Variations of Dose Rate Measured by RAD during the First MSL Martian Year: 2012–
895 2014. *Astrophys. J.*, **810**, 1-24, 2015, DOI: 10.1088/0004-637X/810/1/24.

896 Harri, A-M., M. Genzer, O. Kemppinen, H. Kahanpää, J. Gomez-Elvira, et al. Pressure
897 observations by the Curiosity rover: Initial results, *J. Geophys. Res. – Planet*, **119**, 82-92, 2014,
898 DOI: 10.1002/2013JE004423.

899 Hassler, D.M., C. Zeitlin, R.F. Wimmer-Schweingruber, S. Böttcher, C. Martin, et al. The
900 radiation assessment detector (RAD) investigation. *Space Sci. Rev.*, **170**, 503-558, 2012, DOI:
901 10.1007/s11214-012-9913-1.

902 Hassler, D. M., C. Zeitlin, R.F. Wimmer-Schweingruber, B. Ehresmann, S.C.R. Rafkin, et al.
903 Mars' surface radiation environment measured with the Mars Science Laboratory's Curiosity
904 rover. *Science* **343**, 1244797, 2014, DOI: 10.1126/science.1244797.

905 Huang, C.-L., H.E. Spence, and B.T. Kress. Assessing Access of Galactic Cosmic Rays at
906 Moon's Orbit, *Geophys. Res. Lett.,* **36**, L09109, 2009, DOI: 10.1029/2009GL037916.
907

908 International Commission on Radiological Protection. *ICRP Publication 60: 1990*
909 *Recommendations of the International Commission on Radiological Protection. No. 60.* Oxford:
910 Elsevier Health Sciences, 1991.

911 Iwase, H., K. Niita and T. Nakamura. Development of General-Purpose Particle and Heavy Ion
912 Transport Monte Carlo Code. *J. Nucl. Sci. Technol.*, **39**, 1142-1151, 2002, DOI:
913 10.1080/18811248.2002.9715305.

914 Köhler, J., C. Zeitlin, B. Ehresmann, R. F. Wimmer-Schweingruber, D. M. Hassler, et al.
915 Measurements of the neutron spectrum on the Martian surface with MSL/RAD. *J. Geophys. Res.*
916 *- Planet*, **119**, 594-603, 2014, DOI: 10.1002/2013JE004539.

917 McIlwain, C.E. Coordinates for mapping the distribution of magnetically trapped particles. *J.*
918 *Geophys. Res.*, **66**, 3681–3691, 1961, DOI: 10.1029/JZ066i011p03681.

919 Narici, L., M. Casolino, L. Di Fino, M. Larosa, P. Picozza, V. Zaconte. Radiation survey in the
920 International Space Station. *J. Space Wea. And Space Clim.*, **5**, A37, 2015, DOI:
921 10.1051/swsc/2015037.

922 Narici, L., T. Berger, S. Burmeister, L. Di Fino, A. Rizzo, D. Matthiä, and G. Reitz. Exploiting
923 different active silicon detectors in the International Space Station: ALTEA and DOSTEL
924 galactic cosmic radiation (GCR) measurements. *J. Space Wea. & Space Clim.*, **7**, A18, 2017,
925 DOI: 10.1051/swsc/2017016.

926 Rafkin, S.C.R., C. Zeitlin, B. Ehresmann, D.M. Hassler, J. Guo, et al. Diurnal variations of
927 energetic particle radiation at the surface of Mars as observed by the Mars Science Laboratory
928 Radiation Assessment Detector. *J. Geophys. Res. - Planet*, **119**, 1345–1358, 2014,
929 DOI:10.1002/2013JE004525.

930 Schwadron, N.A., T. Baker, B. Blake, A.W. Case, J.F. Cooper, et al. Lunar radiation
931 environment and space weathering from the Cosmic Ray Telescope for the Effects of Radiation
932 (CRaTER). *J. Geophys. Res.*, **117**, E00H13, 2012, DOI:10.1029/2011JE003978.

933 Simpson, J.A., J.D. Anglin, A. Balogh, M. Bercovitch, J.M. Bouman, et al. The Ulysses cosmic
934 ray and solar particle investigation. *Astron. Astrophys. Suppl. Ser.* **92**, 365-399, 1992.

935 Smart, D.F. and M.A. Shea. A review of geomagnetic cutoff rigidities for earth-orbiting
936 spacecraft. *Adv. Space Res.*, **36**, 2012-2020, 2005, DOI: 10.1016/j.asr.2004.09.015

937 Spence, H.E., A.W. Case, M.J. Golightly, T. Heine, B.A. Larsen, et al. CRaTER: The cosmic ray
938 telescope for the effects of radiation experiment on the lunar reconnaissance orbiter mission.
939 *Space Sci. Rev.* **150**, 243-284, 2010, DOI:10.1007/s11214-009-9584-8.

940 Spence, H.E., C. Joyce, M.D. Looper, N.A. Schwadron, S.S. Smith, L.W. Townsend, and J.K.
941 Wilson. Relative contributions of Galactic Cosmic Rays and lunar proton "albedo" to dose and
942 dose rates near the Moon. *Space Weather*, **11**, 643-650, 2013, DOI: 10.1002/2013SW000995.

943 Stone, E. C., C. M. S. Cohen, W. R. Cook, A. C. Cummings, B. Gauld, B. Kecman, R. A. Leske
944 et al. "The cosmic-ray isotope spectrometer for the advanced composition explorer." In *The*
945 *Advanced Composition Explorer Mission*, pp. 285-356. Springer Netherlands, 1998.

946 Sullivan, J.D. Geometrical factor and directional response of single and multi-element particle
947 telescopes. *Nucl. Instrum. Methods*, **95**, 5–11, 1971, DOI: 10.1016/0029-554X(71)90033-4.

948 Tobias, C.A. Radiation hazards in space flight. No. UCRL-8115. California Univ., Berkeley, CA
949 (US). Radiation Lab., 1958.

950 Wilson, J.W., F.A. Cucinotta, J.L. Shinn, L.C. Simonsen, R.R. Dubey, W.R. Jordan, T.D. Jones,
951 C.K. Chang, and M.Y. Kim. Shielding from solar particle event exposures in deep space. *Radiat.*
952 *Meas.* **30**, 361-382, 1999, DOI: 10.1016/S1350-4487(99)00063-3.

953 Wilson, J.K., H.E. Spence, J. Kasper, M. Golightly, J.B. Blake, et al. The first cosmic ray albedo
954 proton map of the Moon. *J. Geophys. Res. - Planet*, **117**, E00H23, 2012, DOI:
955 10.1029/2011JE003921.

956 Wimmer-Schweingruber, R.F., J. Köhler, D.M. Hassler, J. Guo, J. Appel, et al. On determining
957 the zenith angle dependence of the Martian radiation environment at Gale Crater
958 altitudes. *Geophys. Res. Lett.*, **42**, 2015, DOI: 10.1002/2015GL066664.

959 Zaconte, V., F. Belli, V. Bidoli, M. Casolino, L. Di Fino, et al. ALTEA: the instrument
960 calibration. *Nucl. Instrum. Meth.* **B266**, 2070–2078, 2008, DOI: 10.1016/j.nimb.2008.02.072.

961 Zaconte, V., M. Casolino, L. Di Fino, C. La Tessa, M. Larosa, L. Narici, and P. Picozza. High
962 energy radiation fluences in the ISS-USLab: ion discrimination and particle abundances. *Radiat.*
963 *Meas.*, **45**, 168-172, 2010a, DOI: 10.1016/j.radmeas.2010.01.020.

964 Zaconte, V., M. Casolino, C. De Santis, L. Di Fino, C. La Tessa, M. Larosa, L. Narici, and P.
965 Picozza. The radiation environment in the ISS-USLab measured by ALTEA: spectra and relative
966 nuclear abundances in the polar, equatorial and SAA regions. *Adv. Space Res.*, **46**, 797-799,
967 2010b, DOI: 10.1016/j.asr.2010.02.032.

968 Zeitlin, C., A.W. Case, H.E. Spence, N.A. Schwadron, M. Golightly, et al. Measurements of
969 galactic cosmic ray shielding with the CRaTER instrument. *Space Weather*, **11**.5: 284-296, 2013,
970 doi:10.1002/swe.20043

971 Zeitlin, C., A.W. Case, N.A. Schwadron, H.E. Spence, J.E. Mazur, et al. Solar modulation of the
972 deep space galactic cosmic ray lineal energy spectrum measured by CRaTER, 2009–2014. *Space*
973 *Weather*, **14**, 247–258, 2016, DOI:10.1002/2015SW001314.

974 Zeitlin, C., D.M. Hassler, R.F. Wimmer-Schweingruber, B. Ehresmann, J. Appel, et al.
975 Calibration and Characterization of the Radiation Assessment Detector (RAD) on
976 Curiosity. *Space Sci. Rev.*, **201**, 201-233, 2016, DOI: 10.1007/s1121/s11214-016-0303-y

977 Zeitlin, C., D.M. Hassler, F.A. Cucinotta, B. Ehresmann, R.F. Wimmer-Schweingruber, et al.
978 Measurements of energetic particle radiation in transit to Mars on the Mars Science
979 Laboratory. *Science*, **340**, 1080-1084, 2013, DOI: 10.1126/science.1235989.

980

981
982
983

984

985

986

987

988

989

990

991
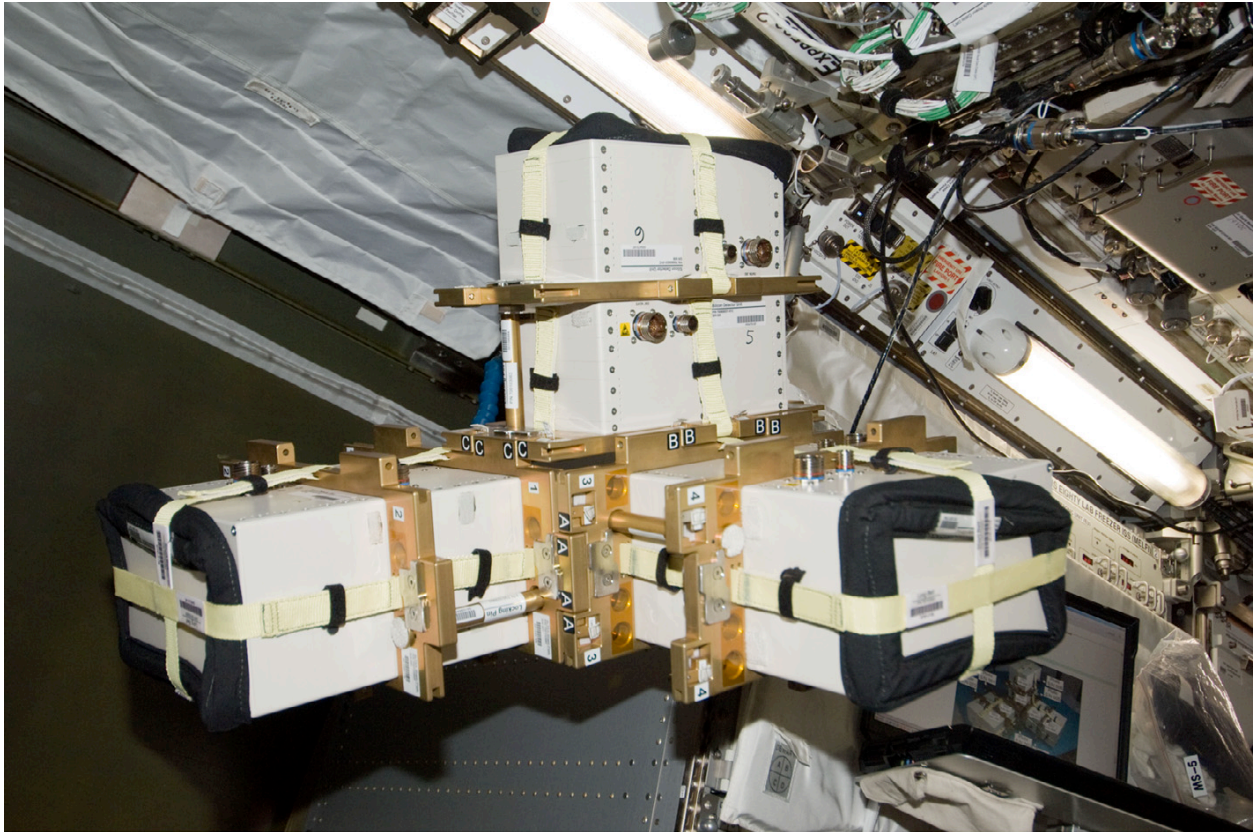
ISS024E015129

Figure 1. ALTEA three-dimensional structure. Each rectangular box contains a particle telescope with a geometric factor of 230 cm^2 sr. When all telescopes are deployed, as they were when ALTEA was station in the USLab, they are arranged to point along the ISS X, Y, and Z directions.
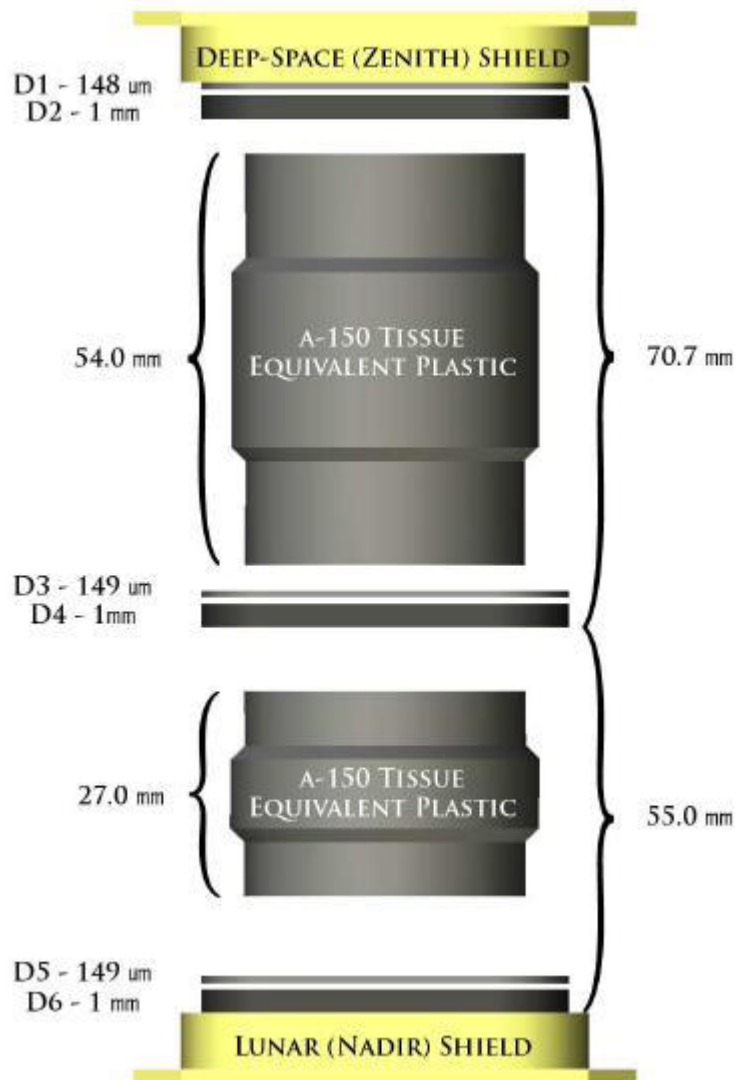
1000
1001
1002

Figure 2. Schematic drawing of the CRaTER telescope. Three pairs of detectors, each containing one thin and one thick detector, are separated by two pieces of tissue-equivalent plastic, allowing for measurements behind shielding for particles coming through the telescope field of view.

1031

1032

1033 TA005038_REVC

1034

1035

1036

1037
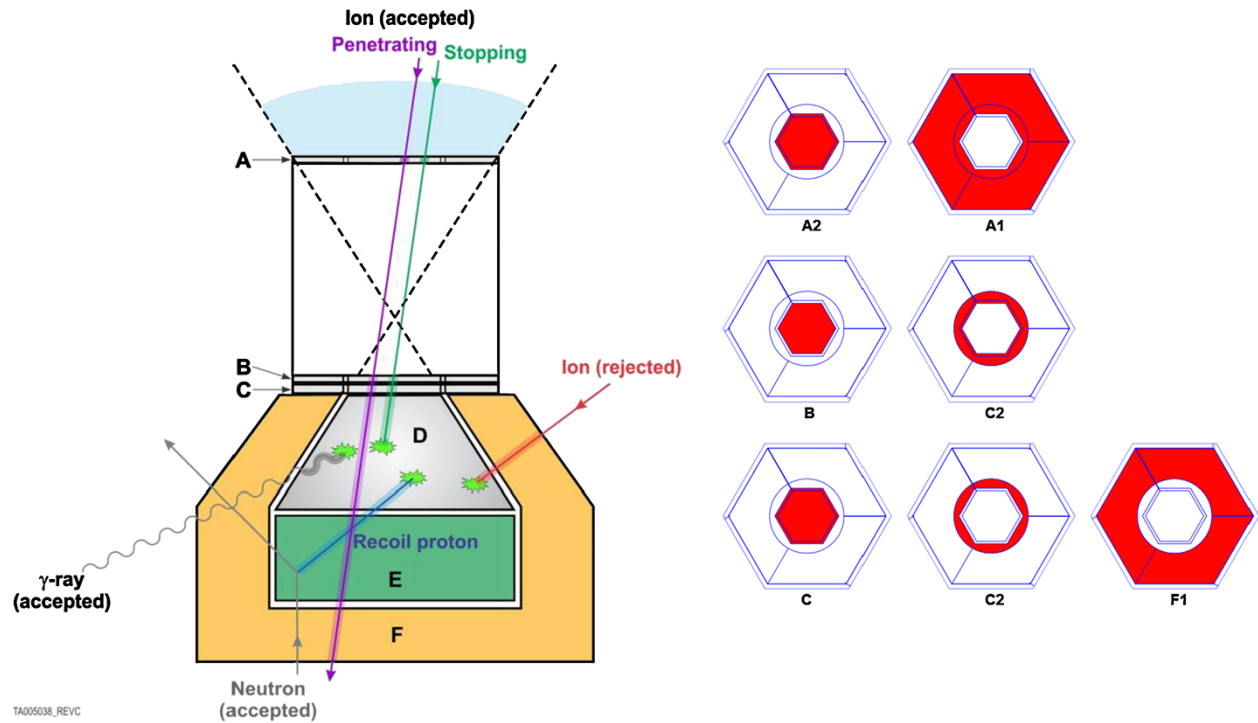
1038 Figure 3. Schematic drawings of the RAD sensor head (left) and that segmented silicon diodes

1039 (right) that comprise the A, B, and C detectors.

1040

1041

1042

1043

1044

1045

1046

Figure 4. Polar plot showing the shielding depth along different rays in the upper hemisphere of RAD's fields of view. The A2*B coincidence cone extends to about 19º in polar angle, while the A1*B cone extends to 30º.
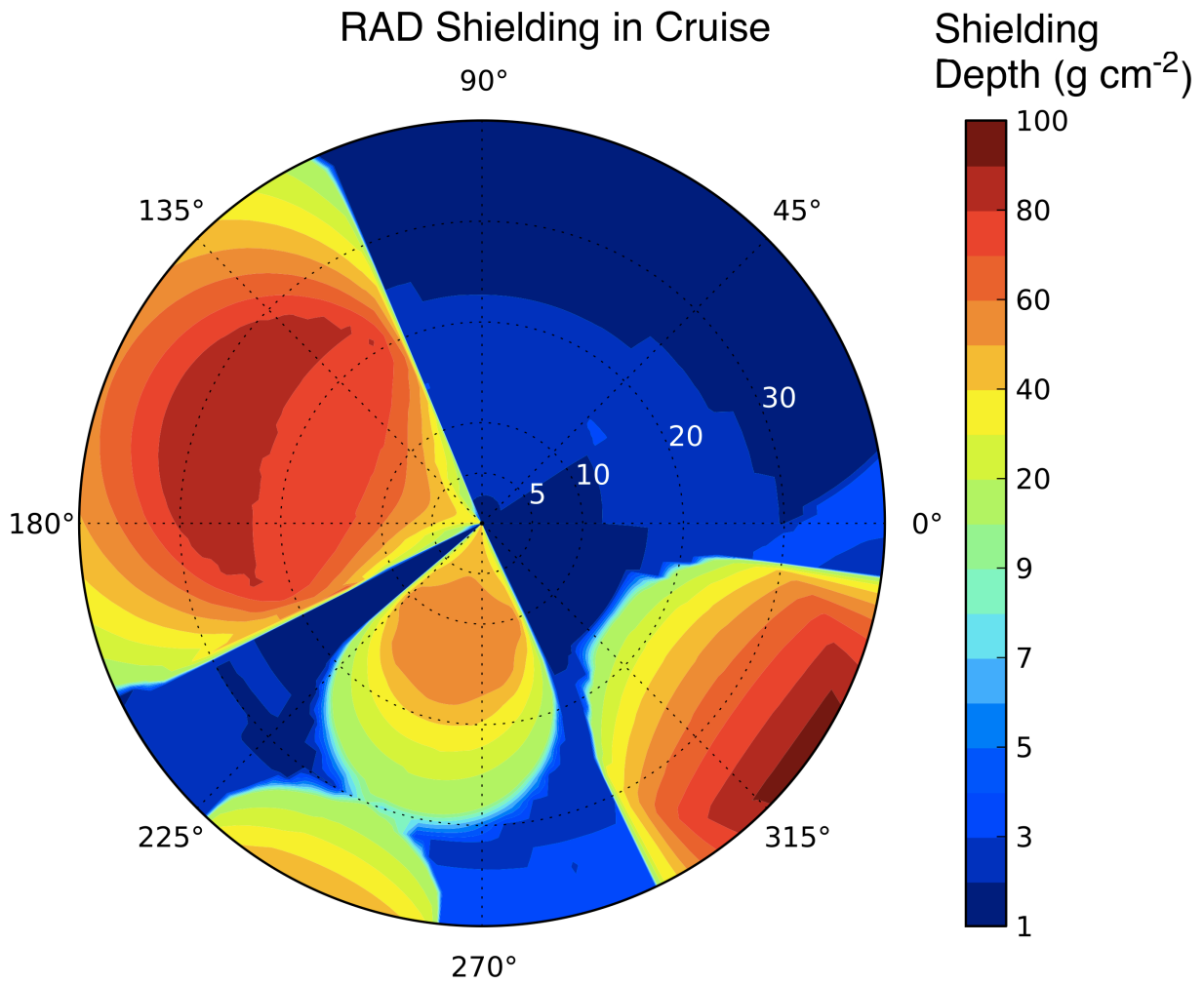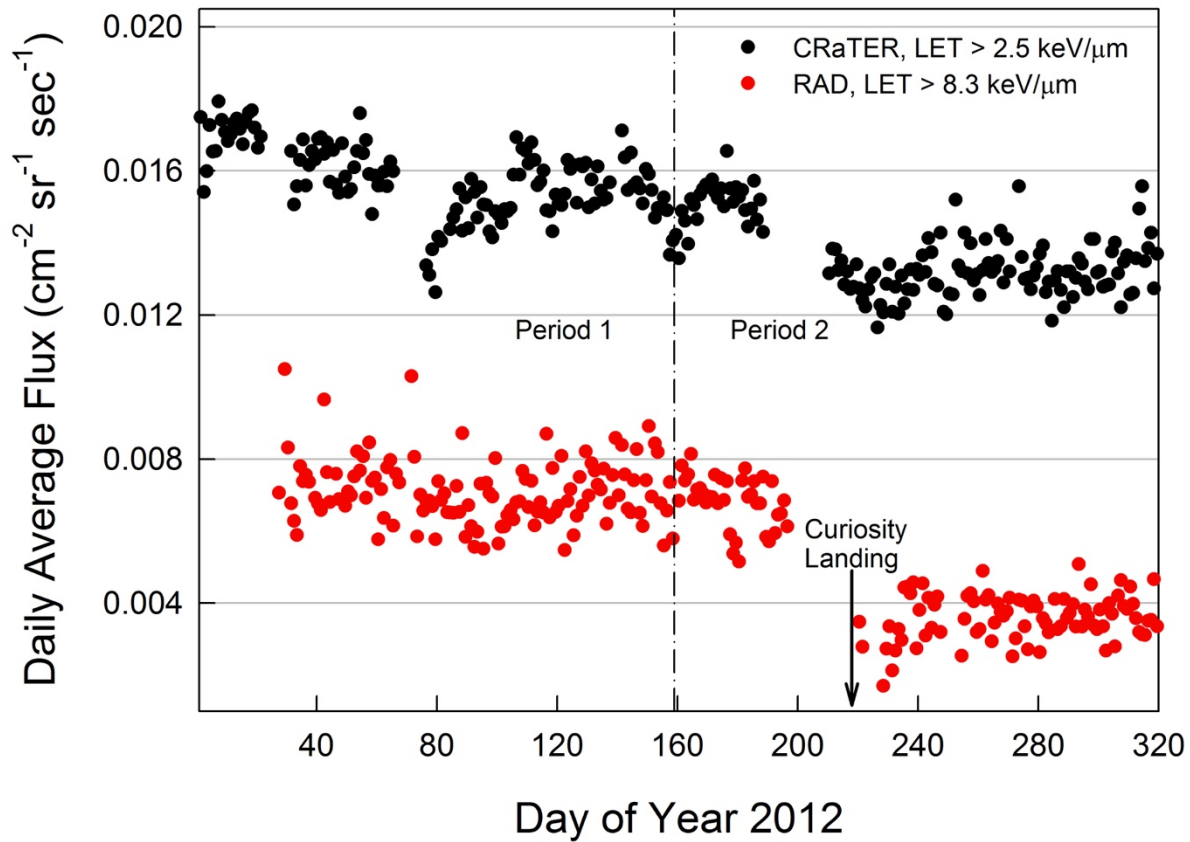
1047

1048

1049

1050

1051

1052

1053

1054

1055

1058
1059
1060

Figure 5. Heavy ion fluxes determined from the RAD heavy-ion counter (8 keV/μm in silicon threshold, in red) and CRaTER (3 keV/μm in silicon threshold, in black). The dashed vertical line indicates the date on which ALTEA was moved from the US Lab to the Columbus module. RAD data from day 220 onwards were obtained after Curiosity landed on Mars. Comparable data from ALTEA can be found in Fig. 5 of Narici et al. (2015).
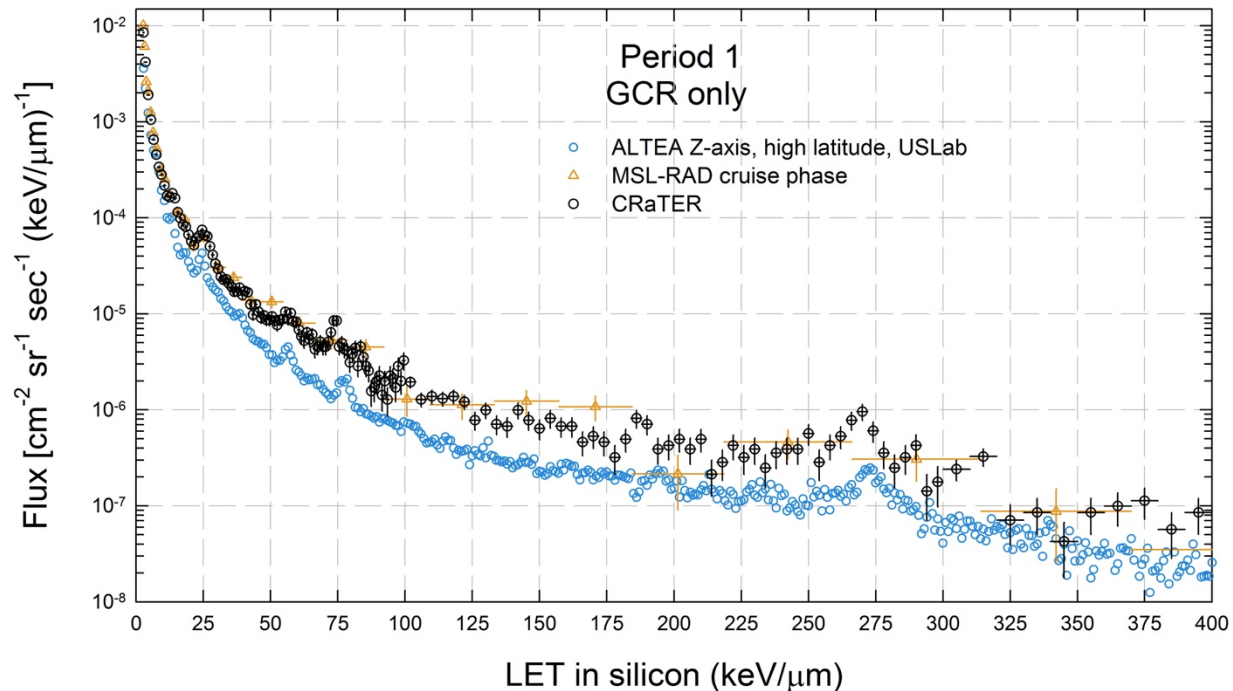
1066
1067
1068
1069
1070

Figure 6. LET spectra of galactic cosmic rays as measured by MSL-RAD, CRaTER, and ALTEA during the earlier of the two measurement periods. CRaTER and ALTEA data are from days 1-159 of 2012, excluding periods of solar activity. ALTEA was located in the USLab module aboard the ISS at this time. MSL-RAD data are from near the end of the transit to Mars, from days 164-196 of 2012. A 3% upward adjustment has been applied to these data to compensate for increased solar modulation in the slightly later time frame.
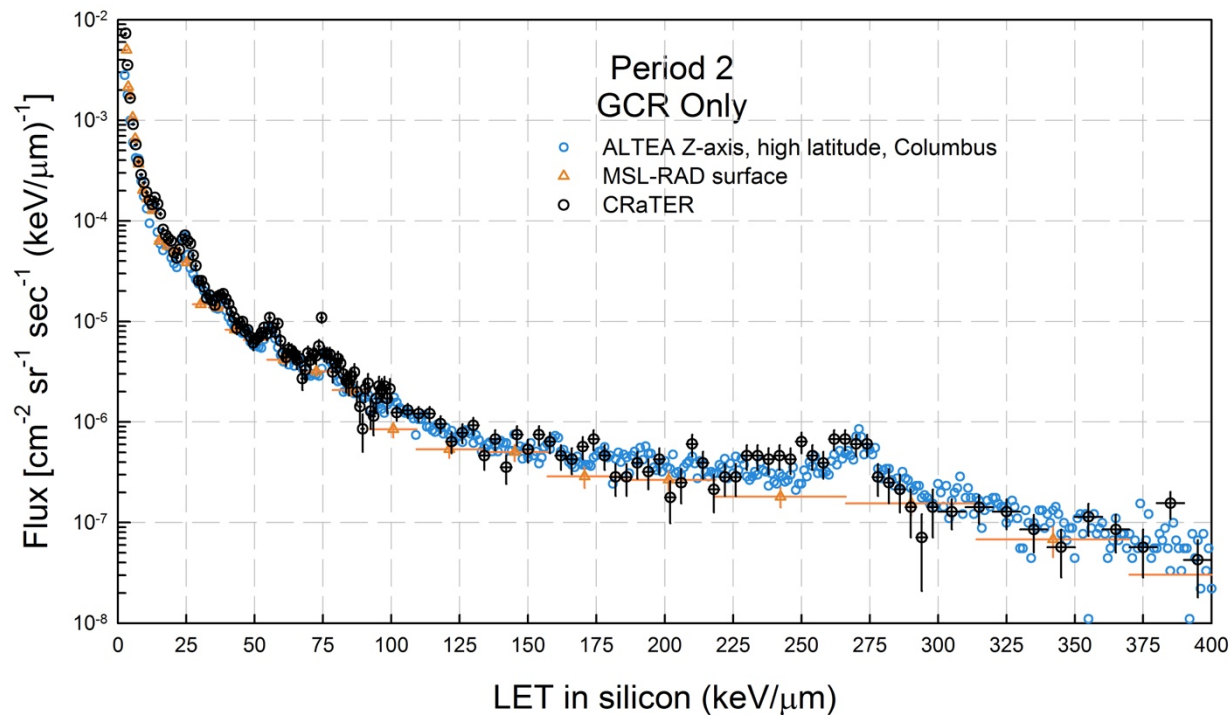
1090

1091
1092
1093
1094
1095 Figure 7. LET spectra of galactic cosmic rays as measured by MSL-RAD, CRaTER, and
1096 ALTEA during the latter measurement period. CRaTER and ALTEA data are from days 160-320
1097 of 2012, again excluding periods of solar activity. ALTEA was located in the Columbus module
1098 aboard the ISS at this time. MSL-RAD data were obtained in Gale Crater on the surface of Mars,
1099 starting at day 220 of 2012.

1100
1101
1102
1103
1104
1105
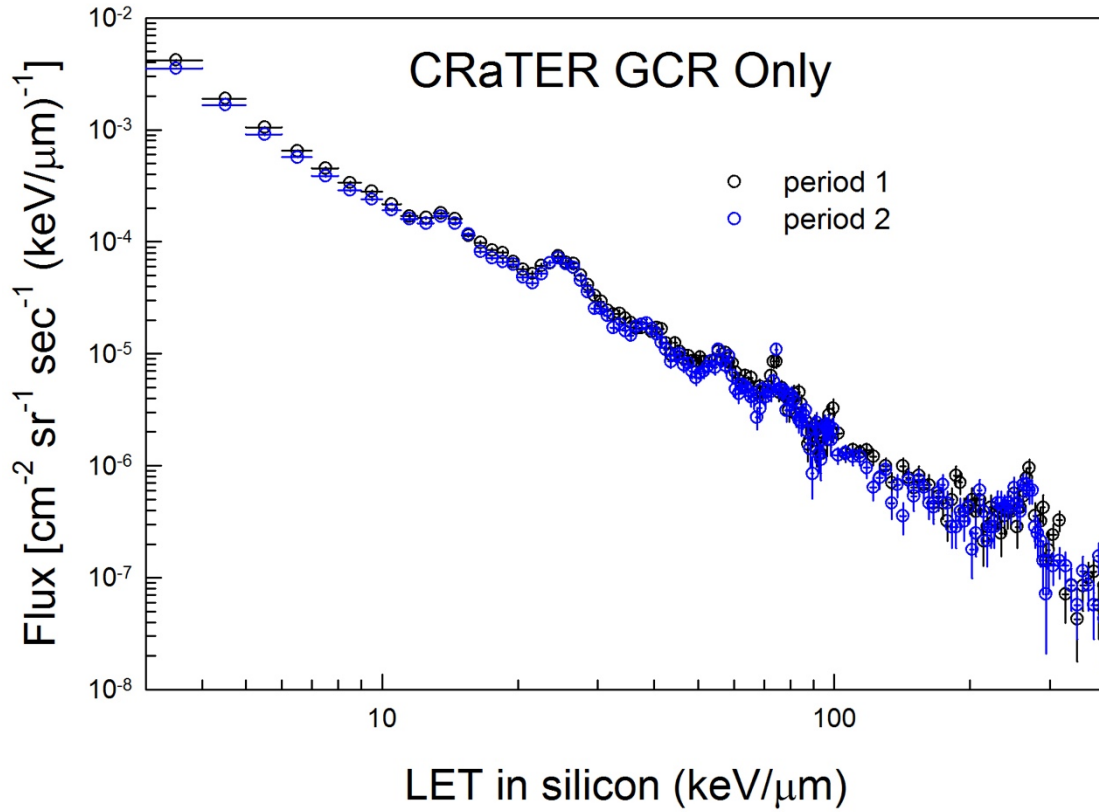1106
1107

1108

1109

1110

1111

1112

1113

1114

Figure 8. LET spectra of galactic cosmic rays as measured by CRaTER, during days 1-159
(black circles) and days 160-320 (blue circles). Data from periods in which solar energetic
particles were present have been excluded.

1118